

Spitzer Deep and Wide Legacy Mid- and Far-Infrared Number Counts and Lower Limits of Cosmic Infrared Background

M. Béthermin¹, H. Dole¹, A. Beelen¹, and H. Aussel²

¹ Institut d'Astrophysique Spatiale (IAS), bat121, F-91405 Orsay, France; Université Paris-Sud 11 and CNRS (UMR8617)

²Laboratoire AIM, CEA/DSM-CNRS-Université Paris Diderot, IRFU/Service d'Astrophysique, Bt. 709, CEA-Saclay, 91191 Gif-sur-Yvette Cedex, France

Accepted for publication in Astronomy & Astrophysics

Abstract

Aims. We want to place stronger lower limits on the Cosmic Infrared Background (CIB) brightness at 24, 70 and 160 μm and measure the extragalactic number counts at these wavelengths in an homogeneous way from various surveys.

Methods. Using *Spitzer* legacy data over 53.6 deg^2 of various depths, we build catalogs with the same extraction method at each wavelength. Completeness and photometric accuracy are estimated with Monte-Carlo simulations. Number count uncertainties are estimated with a counts-in-cells moment method, in order to take into account galaxy clustering. Furthermore, we use a stacking analysis to estimate number counts of sources not detected at 70 and 160 μm . This method is validated by simulations. The integration of the number counts gives new CIB lower limits.

Results. Number counts reach 35 μJy , 3.5 mJy and 40 mJy at 24, 70, and 160 μm , respectively. We reach deeper flux densities of 0.38 mJy at 70, and 3.1 at 160 μm using a stacking analysis. We confirm the number count turnover at 24 and 70 μm , and observe it for the first time at 160 μm at about 20 mJy, together with a power-law behaviour below 10 mJy. These mid- and far-infrared counts: 1) are homogeneously built by combining fields of different depths and sizes, providing a legacy over about three orders of magnitude in flux density; 2) are the deepest to date at 70 and 160 μm ; 3) agree with previous published results in the common measured flux density range; 4) globally agree with the Lagache et al. (2004) model, except at 160 μm where the model slightly overestimates the counts around 20 and 200 mJy.

Conclusions. These counts are integrated to estimate new CIB firm lower limits of $2.29^{+0.09}_{-0.09}$, $5.4^{+0.4}_{-0.4}$, and $8.9^{+1.1}_{-1.1} \text{ nW.m}^{-2}.\text{sr}^{-1}$ at 24, 70, and 160 μm , respectively, and extrapolated to give new estimates of the CIB due to galaxies of $2.86^{+0.19}_{-0.16}$, $6.6^{+0.7}_{-0.6}$, and $14.6^{+7.1}_{-2.9} \text{ nW.m}^{-2}.\text{sr}^{-1}$, respectively. Products (PSF, counts, CIB contributions, software) are publicly available for download at <http://www.ias.u-psud.fr/irgalaxies/>.

Key words. Cosmology: observations - Cosmology: diffuse radiation - Galaxies: statistics - Galaxies: evolution - Galaxies: photometry - Infrared: galaxies

1. Introduction

The Extragalactic Background Light (EBL) is the relic emission of all processes of structure formation in the Universe. About half of this emission, called the Cosmic Infrared Background (CIB) is emitted in the 8-1000 μm range, and peaks around 150 μm . It is essentially due to the star formation (Puget et al. 1996; Fixsen et al. 1998; Hauser et al. 1998; Lagache et al. 1999; Gispert et al. 2000; Hauser & Dwek 2001; Kashlinsky 2005; Lagache et al. 2005).

The CIB Spectral Energy Distribution (SED) is an important constraint for the infrared galaxies evolution models (e.g. Lagache et al. (2004); Franceschini et al. (2009); Le Borgne et al. (2009); Pearson & Khan (2009); Rowan-Robinson (2009); Valiante et al. (2009)). It gives the budget of infrared emission since the first star. The distribution of flux of sources responsible of this background is also a critical constraint. In this paper, we propose to measure the level of the CIB and the flux distribution of the sources at 3 wavelengths (24, 70 and 160 μm).

In 1980's, the Infrared Astronomical Satellite (IRAS) and COBE/DIRBE performed the first Mid-InfraRed (MIR) and Far-infraRed (FIR) full-sky surveys. Nevertheless, the detected

sources were responsible of a very little part of the CIB. Between 1995 and 1998, ISO (Infrared Space Observatory) performed deeper observations of infrared galaxies. Elbaz et al. (2002) resolved into source more than half of the CIB at 15 μm . At larger wavelength, the sensitivity and the angular resolution was not sufficient to resolve the CIB (Dole et al. 2001).

The Spitzer Space Telescope (Werner et al. 2004), launched in 2003, has performed deep infrared observations on wide fields. The Multiband Imaging Photometers for Spitzer (MIPS) (Rieke et al. 2004) mapped the sky at 24, 70 and 160 μm . About 60% of CIB was resolved at 24 μm (Papovich et al. 2004) and at 70 μm (Frayser et al. 2006). Because of confusion (Dole et al. 2003), only about 7% was resolved at 160 μm (Dole et al. 2004). Dole et al. (2006) managed to resolve most of 70 and 160 μm by stacking 24 μm sources.

The cold mission of Spitzer is over, and lots of data are now public. In this paper, we present extragalactic number counts built homogeneously combining deep and wide fields. The large sky surface used significantly reduces uncertainties on number counts. In order to obtain very deep FIR number counts, we use a stacking analysis. Using these counts, we estimate the level of

Field name	Surface area			80% completeness flux			Scaling factor		
	24 μm	70 μm	160 μm	24 μm	70 μm	160 μm	24 μm	70 μm	160 μm
	deg ²			μJy	mJy				
FIDEL eCDFS	0.23	0.19	-	60.	4.6	-	1.0157	1	-
FIDEL EGS	0.41	-	0.38	76.	-	45.	1.0157	-	0.93
COSMOS	2.73	2.41	2.58	96.	7.9	46.	1	0.92	0.96
SWIRE LH	10.04	11.88	11.10	282.	25.4	92.	1.0509	1.10	0.93
SWIRE EN1	9.98	9.98	9.30	261.	24.7	94.	1.0509	1.10	0.93
SWIRE EN2	5.36	5.34	4.98	267.	26.0	90.	1.0509	1.10	0.98
SWIRE ES1	7.45	7.43	6.71	411.	36.4	130.	1.0509	1.10	0.98
SWIRE CDFS	8.42	8.28	7.87	281.	24.7	88.	1.0509	1.10	0.98
SWIRE XMM	8.93	-	-	351.	-	-	1.0509	-	-
Total	53.55	45.51	42.91						

Table 1. Size, 80% completeness flux density and calibration scaling factor (see section 2.1) of the used fields. Some fields are not used at all wavelengths.

the CIB in the 3 MIPS bands.

2. Data, source extraction and photometry

2.1. Data

We use the public *Spitzer* mosaics¹ from different observation programs: GOODS/FIDEL (PI: M. Dickinson), COSMOS (PI: D. Sanders) and SWIRE (PI: C. Lonsdale). We use only the central part of each field by using a cut of 50% of the median coverage for SWIRE fields and 80 % for the other fields. The total area covers 53.6, 45.5, 42.9 deg² at respectively 24, 70 and 160 μm . The surface of the deep fields (FIDEL, COSMOS) is about 3.5 deg². Some fields are not used at all wavelength for different reasons: There is no public release of FIDEL CDFS data at 160 μm ; the pixels of the EGS 70 μm are not square; XMM is not observed at 70 and 160 μm . Table 1 summarises field names, sizes and completenesses.

In 2006, new calibration factors have been adopted for MIPS (Engelbracht et al. 2007; Gordon et al. 2007; Stansberry et al. 2007). The conversion factor from instrumental unit to MJy/sr is 0.0454 (resp. 702 and 41.7) at 24 μm (resp. 70 and 160 μm). The COSMOS GO3 and SWIRE (released 22 Dec. 2006) mosaics were generated with the new calibration. The FIDEL mosaics are obtained with other factors at 24 and 160 μm (resp. 0.0447 and 44.7). The 70 and 160 μm COSMOS mosaics are color corrected (see section 2.3). Consequently, before source extraction, we apply a scaling factor (see table 1) to each mosaic in order to work on an homogeneous sample of maps (new calibration and no color correction).

2.2. Source extraction and photometry

The goal is to build homogeneous number counts with well controlled systematics and high statistics. However, the fields present various sizes and depths. We thus use a single extraction method at a given wavelength, allowing to combine the heterogeneous datasets in a coherent way.

2.2.1. Mid-IR/Far-IR differences

The MIR (24 μm) and FIR (70 and 160 μm) maps have different properties: in the MIR, we observe lots of faint blended sources; in the FIR, due to confusion (Dole et al. 2004), all these faint blended sources are only seen as background fluctuations. Consequently, we use different extraction and photometry methods for each wavelength. In the MIR, the priority is the deblending: we thus use SExtractor (Bertin & Arnouts 1996) and PSF fitting. In the FIR, we use methods efficient with strong background fluctuations: wavelet filtering, threshold detection and aperture photometry.

2.2.2. Point Spread Function (PSF)

The 24 μm empirical PSF of each field is generated with the IRAF (Image Reduction and Analysis Facility²) DAOPHOT package (Stetson 1987) on the 30 brightest sources of each map. It is normalised in a 12 arcsec radius aperture. Aperture correction (1.19) is computed using S Tiny Tim³ (Krist 2006) theoretical PSF for a constant νS_ν spectrum. The difference of correction between a $S_\nu = \nu^{-2}$ and a ν^2 spectrum is less than 2%. So, the hypothesis on the input spectrum is not critical for the PSF normalisation.

At 70 and 160, we build a single empirical PSF from the SWIRE fields. We use the Starfinder PSF extraction routine (Diolaiti et al. 2000) which median-stacks the brightest non-saturated sources (100 mJy < S_{70} < 10 Jy and 300 mJy < S_{160} < 1 Jy). Previously, fainter neighboring sources have been subtracted using a first estimation of the PSF. At 70 (resp. 160) μm , the normalisation is done in a 35 (resp. 80) arcsec aperture, with a sky annulus between 75 and 125 (resp. 150 and 250) arcsec; the aperture correction is 1.21 (resp. 1.20). Theoretical signal in the sky annulus and aperture correction are computed using S Tiny Tim *Spitzer* PSF for a constant νS_ν spectrum. These parameters do not vary more than 5 % with the spectrum of sources. Pixels affected by the temporal median filtering artifact, sometimes present around bright sources, are masked prior to these operations.

¹ from the *Spitzer* Science Center website: <http://data.spitzer.caltech.edu/popular/>

² <http://iraf.noao.edu/>

³ <http://ssc.spitzer.caltech.edu/archanally/contributed/stinytim/>

2.2.3. Source extraction and photometry

At 24 μm , we detect sources with SExtractor. We choose a gaussian filter (gauss_5.0_9x9.conv) and a background filter size of 64×64 pixels. The detection and analysis thresholds are tuned for each field. DAOPHOT allstar routine performs PSF fitting photometry. This routine is very efficient for blended sources flux measurement.

At 70 and 160 μm , we apply the a-trou wavelet filtering (Starck et al. 1999) on the maps to remove the large scale fluctuations (10 pixels) on which we perform the source detection with a threshold algorithm (Dole et al. 2001, 2004). The threshold is tuned for each field. Photometry is done by aperture photometry on non-filtered map at the positions found on the wavelet-filtered map. At 70 μm , we use 10 arcsec aperture radius and a 18 to 39 arcsec sky annulus. At 160 μm , we use an aperture of 20 arcsec and a 40 to 75 arcsec annulus. Aperture correction are computed using the normalised empirical PSF: 3.22 at 70 and 3.60 at 160 μm . In order to estimate the uncertainty on this correction, aperture corrections are computed using 5 PSF built on 5 different SWIRE fields. The uncertainty is 1.5% at 70 μm and 4.5% at 160.

2.3. Color correction

The MIPS calibration factors are calculated for a 10000 K blackbody (MIPS Data Handbook 2007⁴). However, galaxies SED (Spectral Energy Distribution) are different and the MIPS photometric bands are large ($\lambda/\Delta\lambda \approx 3$). Thus, color corrections are needed. We use (like Shupe et al. (2008) and Frayer et al. (2009)) a constant νS_ν spectrum at 24, 70 and 160 μm . Consequently, all flux are divided by 0.961, 0.918 and 0.959 at 24, 70 and 160 μm due to this color correction. An other possible convention is $\nu S_\nu \propto \nu^{-1}$. This convention is more relevant for the local sources at 160 μm , whose spectrum decreases quickly with wavelength. Nevertheless, the redshifted sources studied by stacking are seen at their peak of the cold dust emission, and their SED are more in agreement with the constant νS_ν convention. The difference of color correction between these two conventions is less than 2 %, and this choice is thus not critical. We consequently choose the constant νS_ν convention to compare more easily our results with Shupe et al. (2008) and Frayer et al. (2009).

3. catalog properties

3.1. Spurious sources

Our statistical analysis may suffer from spurious sources. We have to estimate how many false detections are present in a map and what is their flux distribution. To do so, we build a catalog using the flipped map. To build this flipped map, we multiply the values of the pixels of the original map by a factor -1. Detection and photometry parameters are exactly the same as for normal catalogs. At 24 μm , there are few spurious sources ($< 10\%$) in bins brighter than the 80% completeness limit flux density. At 70 and 160 μm , fluctuations of the background due to unresolved faint sources are responsible for spurious detections. Nevertheless, the ratio between detected sources number and fake sources number stays reasonable (below 0.2)

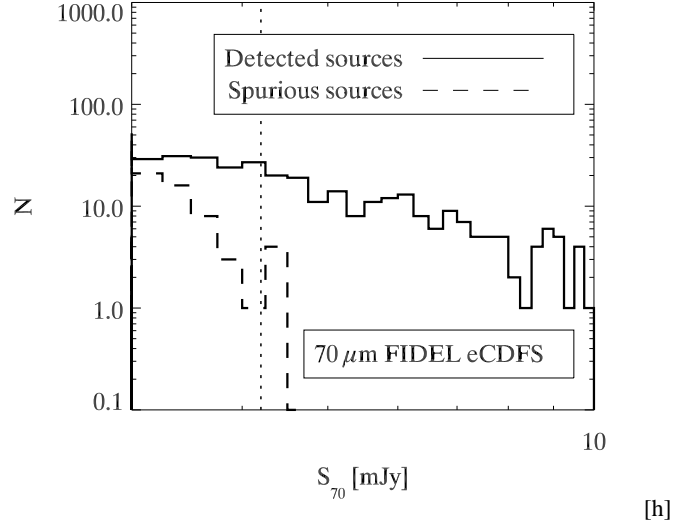


Figure 1. Flux distribution of sources extracted from normal (solid line) and flipped (dash line) maps, at 70 μm in FIDEL eCDFs. The vertical dashed line represents the 80% completeness flux density.

down to the 80% completeness limit (see example of FIDEL CDFS at 70 μm in figure 1).

3.2. Completeness

The completeness is the probability to extract a source of a given flux. In order to estimate it, we add artificial sources (based on empirical PSF) on the initial map and look for a detection in a 2 arcsec radius at 24 μm around initial position (8 arcsec at 70 and 16 arcsec at 160 μm). This operation is done for different fluxes with a Monte-Carlo simulation. We choose the number of artificial sources in each realization so that they have less than 1% probability to fall at a distance shorter than 2 PSF FWHM (Full Width at Half Maximum). Completeness is plotted in figure 2 and the 80% completeness level is reported in table 1.

3.3. Photometric accuracy

The photometric accuracy is checked with the same Monte-Carlo simulation. For different input fluxes, we build histograms of measured fluxes and compute the median and scatter of these distributions. At lower fluxes, fluxes are overestimated and errors are larger. These informations are used to estimate the Eddington bias (see next section). Photometric accuracy at 70 μm in FIDEL CDFS is plotted as an example in figure 3.

We also compare our catalogs with published catalogs. At 24 μm , we compare with the GOODS CDFS catalog of Chary et al. (2004), and the COSMOS catalog of LeFloc'h et al. (2009). Their fluxes are multiplied by a corrective factor to be compatible with $\nu S_\nu = \text{constant}$ convention. Sources are considered to be the same if they are separated by less than 2 arcsec. We compute the standard deviation of the distribution of the ratio between our and their catalogs. In a 80-120 μJy bin in the CDFS, we find a dispersion of 19%. In a 150-250 μJy

⁴ <http://ssc.spitzer.caltech.edu/mips/dh/>

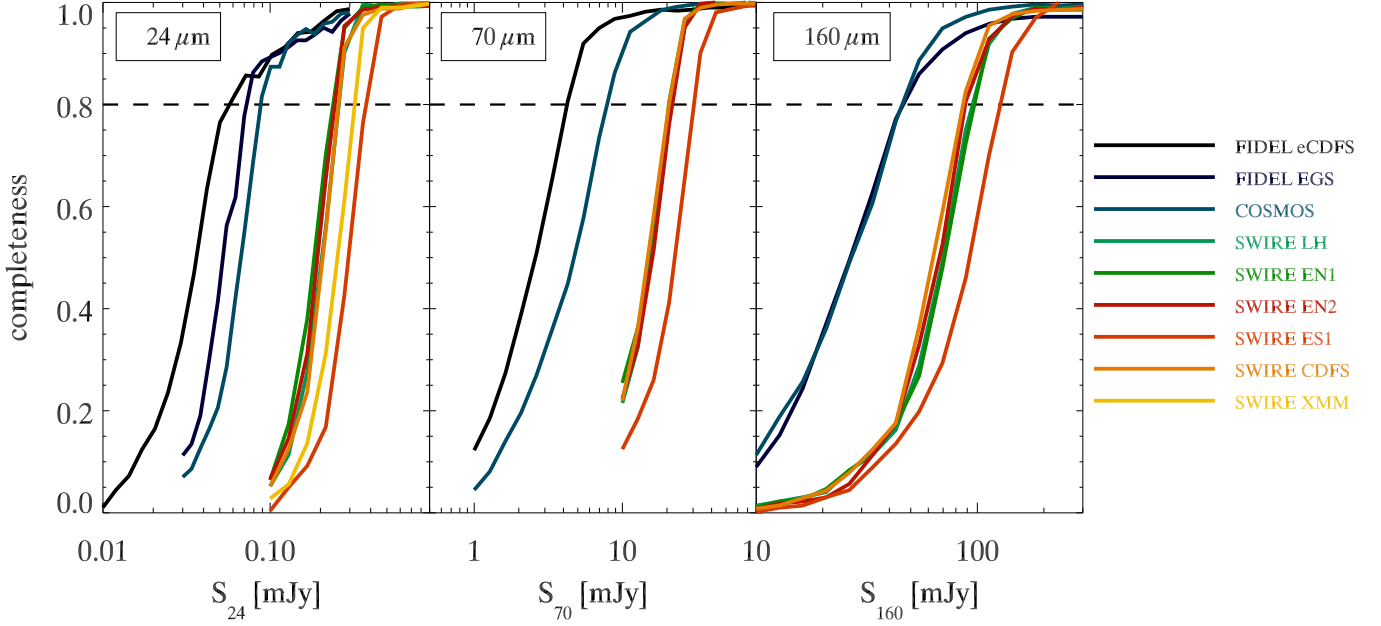


Figure 2. Completeness at 24 (left), 70 (center), and 160 μm (right) as a function of source flux, for all the fields. The dashed line represents 80% completeness.

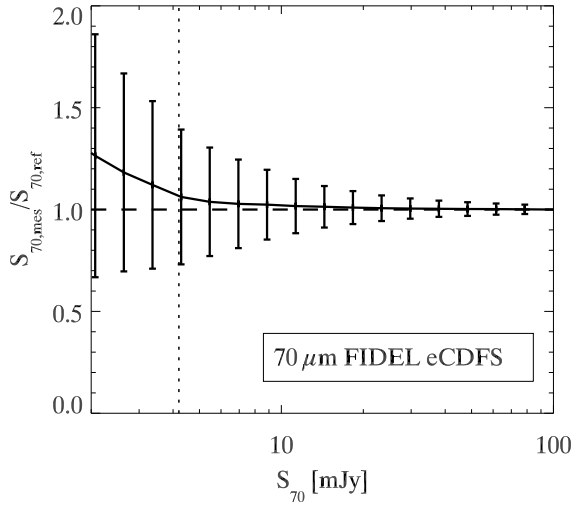


Figure 3. Ratio between measured flux and input flux computed from Monte Carlo simulations, at 70 μm in FIDEL eCDFs. Error bars represent 1σ dispersion. The vertical dashed line represents the 80% completeness flux density.

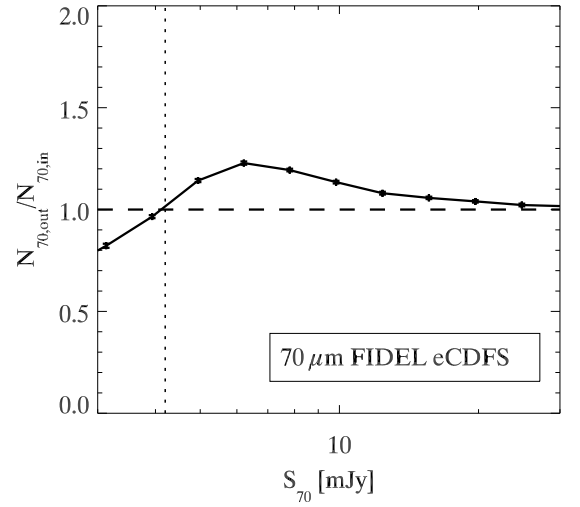


Figure 4. Eddington bias: ratio between number of detected sources and number of input sources, at 70 μm in FIDEL eCDFs. The vertical dashed line represents the 80% completeness flux density.

bin in COSMOS, we find a scatter of 13%. The offset is +3% with COSMOS catalog and -1% with GOODS catalog. Our At 70 and 160 μm , we compare our catalogs with COSMOS and SWIRE team ones. In all cases, the scatter is less than 15%, and the offset is less than 3%. At all wavelength and for all field, the offset is less than calibration uncertainty.

3.4. Eddington bias

When sources become fainter, photometric errors increase. In addition, fainter sources are more numerous than brighter ones (in general $dN/dS \sim S^{-\gamma}$). Consequently, the number of sources in faint bins are overestimated. This is the classical Eddington bias (Eddington 1913, 1940). The example of FIDEL CDFS at 70 μm is plotted in figure 4.

In order to correct for this effect at 70 and 160 μm , we estimate a correction factor for each flux bin. We generate an

input flux catalog with a power-law distribution ($r = 1.6$ at $70 \mu\text{m}$, $r = 3$ at $160 \mu\text{m}$). We take into account completeness and photometric errors (coming from Monte-Carlo simulations) to generate a mock catalog. We then compute the ratio between the number of mock sources found in a bin and the number of input sources. This task is done for all fields. This correction is more important for large r (at $160 \mu\text{m}$). At $24 \mu\text{m}$, thanks to PSF fitting, photometric error is more reduced and symmetrical. Less faint sources are thus placed in brighter flux bins. Thanks to this properties and the low r (about 1.45), this correction can be ignored for $24 \mu\text{m}$ counts.

4. Number counts

4.1. Removing stars from the catalogs

To compute extragalactic number counts at $24 \mu\text{m}$, we remove the stars using a $K - [24] < 2$ color criteria and identification procedure following Shupe et al. (2008). The K band magnitude comes from the 2MASS catalog (Skrutskie et al. 2006). We ignore the star contribution at 70 and $160 \mu\text{m}$, which is negligible ($< 1\%$ in all used flux density bins) according DIRBE Faint Count model (Arendt et al. 1998).

4.2. $24 \mu\text{m}$ number counts

For each field, in each flux bin, we count the number of extragalactic sources. We subtract the number of spurious detections (performed on the flipped map). We divide by the completeness. Next, the counts of all fields are combined together using a mean weighted by field size. In fact, a weighting by the number of sources in each field overweights the denser fields and biases the counts. Counts from a field are combined only if the lower end of the flux bin is larger or equal than the 80% completeness. We thus reach $71 \mu\text{Jy}$ (71 to $90 \mu\text{Jy}$ bin) in the counts. However, in order to probe fainter flux densities, we use the data from the deepest field (FIDEL eCDFs) between 50 and 80 % completeness, allowing to reach $35 \mu\text{Jy}$.

Our number counts are plotted in figure 5 and written in table 2. We also plot data from Papovich et al. (2004), Shupe et al. (2008) and LeFloc'h et al. (2009), and model predictions from Lagache et al. (2004) and Le Borgne et al. (2009). Papovich et al. (2004) fluxes are multiplied by a factor 1.052 to take into account the update in the calibration, the color correction and the PSF. This correction of flux also imply a correction on number counts, following the formula:

$$\left(\frac{dN}{dS_f} S_f^{2.5}\right)_{S_f} = \left(c^{1.5} \frac{dN}{dS_i} S_i^{2.5}\right)_{cS_i} \quad (1)$$

where S_i is the initial flux, S_f is the corrected flux and c the corrective factor ($S_f = cS_i$). A correction of flux thus corresponds to a shift in abscissa (factor c) and in ordinate (factor $c^{1.5}$). They do not subtract stars and thus overestimate counts above 10 mJy. We have a very good agreement with this work below 10 mJy. We have also a very good agreement with Shupe et al. (2008). The LeFloc'h et al. (2009) fluxes are multiplied by 1.05 to take into account a difference of reference SED: 10 000K versus constant νS_ν , and by an other correction of 3% corresponding to the offset observed in section 3.3). There is an excellent agreement with their work.

The Lagache et al. (2004)⁵ and Le Borgne et al. (2009)⁶ are in general good agreement with the data, in particular on the faint end below $100 \mu\text{Jy}$, and on the position of the peak around $300 \mu\text{Jy}$. However, the Lagache et al. (2004) model slightly underestimates (about 10%) the counts above $200 \mu\text{Jy}$. The Le Borgne et al. (2009) model is flatter than the data, and agrees reasonably well above $600 \mu\text{Jy}$.

4.3. $70 \mu\text{m}$ number counts

Counts in the flux density bins brighter than the 80% completeness limit, are obtained in the same way as at $24 \mu\text{m}$ (figure 6 and table 3). In addition, they are corrected from the Eddington bias (c.f. 3.4). We reach about 4.9 mJy at 80% completeness (4.9 to 6.8 bin). We use CDFS below 80% completeness limit to probe fainter flux density level. We cut these counts at 3.5 mJy. At this flux density, the spurious rate reach 50%. We use a stacking analysis to probe fainter flux density levels (c.f. section 5).

We can see breaks in the counts around 10 and 20 mJy. These breaks appear between points built with a different set of fields. Our counts agree with earlier works of Dole et al. (2004), Frayer et al. (2006) and Frayer et al. (2009). However, these works suppose only a poissonian uncertainty, which underestimates the error bars (see section 4.5). We also are in good agreement with these works. The Lagache et al. (2004) model is in good agreement with our data. The Le Borgne et al. (2009) model gives a reasonable fit, despite an excess of about 30% between 3 and 10 mJy.

4.4. $160 \mu\text{m}$ number counts

The $160 \mu\text{m}$ number counts are obtained exactly in the same way as at $70 \mu\text{m}$. We use COSMOS and EGS to probe counts below 80% completeness limit. We reach 51 mJy at 80% completeness (51 to 66 mJy bin) and 40 mJy for 50% spurious rate cut (figure 7 and table 4). We use a stacking analysis to probe fainter flux density levels (c.f. section 5).

Our counts agree with earlier works of Dole et al. (2004) and Frayer et al. (2009). We find, like Frayer et al. (2009), that Lagache et al. (2004) model overestimates the counts by about 30% above 50 mJy (see discussion in section 7.2). On the contrary, the Le Borgne et al. (2009) model underpredicts the counts by about 20% between 50 and 150 mJy.

4.5. Uncertainties on number counts including clustering

Shupe et al. (2008) have shown that the SWIRE field-to-field variance is significantly higher than Poisson noise (by a factor of 3 in some flux bins). They estimate their uncertainties on number counts using a field bootstrap method. We use a more formal method to deal with this problem.

⁵ Lagache et al. (2004) model use a ΛCDM cosmology with $\Omega_\Lambda=0.73$, $\Omega_M=0.27$ and $h = 0.71$

⁶ Le Borgne et al. (2009) model use a ΛCDM cosmology with $\Omega_\Lambda=0.7$, $\Omega_M=0.3$ and $h = 0.7$

$\langle S \rangle$	S_{min}	S_{max}	$dN/dS.S^{2.5}$	$\sigma_{poisson}$	$\sigma_{clustering}$	$\sigma_{clus.+calib.}$	Ω_{used}
(in mJy)				(in gal.Jy ^{1.5} .sr ⁻¹)			deg ²
0.040	0.035	0.044	17.5	1.0	1.1	1.3	0.2
0.050	0.044	0.056	21.4	1.0	1.1	1.4	0.2
0.064	0.056	0.071	28.2	1.2	1.5	1.8	0.2
0.081	0.071	0.090	36.2	1.5	1.9	2.4	0.2
0.102	0.090	0.114	52.6	1.3	1.9	2.9	0.6
0.130	0.114	0.145	64.1	1.0	1.7	3.1	3.4
0.164	0.145	0.184	78.7	1.1	2.2	3.8	3.4
0.208	0.184	0.233	89.8	1.3	2.8	4.5	3.4
0.264	0.233	0.295	96.5	1.5	3.3	5.1	3.4
0.335	0.295	0.374	112.0	0.8	1.8	4.8	37.2
0.424	0.374	0.474	103.7	0.6	1.7	4.5	46.1
0.538	0.474	0.601	91.9	0.6	1.5	4.0	53.6
0.681	0.601	0.762	81.2	0.6	1.5	3.6	53.6
0.863	0.762	0.965	72.8	0.7	1.6	3.3	53.6
1.094	0.965	1.223	65.3	0.8	1.6	3.1	53.6
1.387	1.223	1.550	60.8	0.9	1.7	3.0	53.6
1.758	1.550	1.965	56.7	1.0	1.8	2.9	53.6
2.228	1.965	2.490	55.4	1.2	2.1	3.0	53.6
2.823	2.490	3.156	54.0	1.5	2.3	3.2	53.6
3.578	3.156	4.000	55.9	1.8	2.7	3.5	53.6
5.807	4.000	7.615	54.8	1.5	2.9	3.6	53.6
11.055	7.615	14.496	46.9	2.3	3.6	4.1	53.6
21.045	14.496	27.595	36.4	3.3	4.4	4.6	53.6
40.063	27.595	52.531	43.4	5.9	7.7	7.9	53.6
76.265	52.531	100.000	47.7	9.9	12.0	12.2	53.6

Table 2. Differential number counts at 24 μm . $\sigma_{clustering}$ is uncertainty taking into account clustering (see section 4.5). $\sigma_{clus.+calib.}$ take into accounts both clustering and calibration (Engelbracht et al. 2007).

$\langle S \rangle$	S_{min}	S_{max}	$dN/dS.S^{2.5}$	$\sigma_{poisson}$	$\sigma_{clustering}$	$\sigma_{clus.+calib.}$	Ω_{used}
(in mJy)				(in gal.Jy ^{1.5} .sr ⁻¹)			deg ²
4.197	3.500	4.894	2073.	264.	309.	342.	0.2
5.868	4.894	6.843	2015.	249.	298.	330.	0.2
8.206	6.843	9.569	1690.	289.	332.	353.	0.2
11.474	9.569	13.380	2105.	123.	202.	250.	2.6
16.044	13.380	18.708	2351.	148.	228.	281.	2.6
22.434	18.708	26.159	1706.	153.	208.	240.	2.6
31.369	26.159	36.578	2557.	69.	124.	218.	38.1
43.862	36.578	51.146	2446.	73.	123.	211.	45.5
61.331	51.146	71.517	2359.	90.	141.	217.	45.5
85.758	71.517	100.000	2257.	112.	164.	228.	45.5
157.720	100.000	215.440	2354.	121.	198.	257.	45.5
339.800	215.440	464.160	2048.	200.	276.	311.	45.5
732.080	464.160	1000.000	2349.	381.	500.	526.	45.5

Table 3. Differential number counts at 70 μm . $\sigma_{clustering}$ is uncertainty taking into account clustering (see section 4.5). $\sigma_{clus.+calib.}$ take into accounts both clustering and calibration (Gordon et al. 2007).

$\langle S \rangle$	S_{min}	S_{max}	$dN/dS.S^{2.5}$	$\sigma_{poisson}$	$\sigma_{clustering}$	$\sigma_{clus.+calib.}$	Ω_{used}
(in mJy)				(in gal.Jy ^{1.5} .sr ⁻¹)			deg ²
45.747	40.000	51.493	16855.	1312.	2879.	3519.	3.0
58.891	51.493	66.289	14926.	1243.	2704.	3243.	3.0
75.813	66.289	85.336	13498.	1319.	2648.	3104.	3.0
97.596	85.336	109.860	12000.	1407.	2442.	2835.	3.0
125.640	109.860	141.420	10687.	457.	991.	1621.	36.2
161.740	141.420	182.060	7769.	425.	773.	1211.	42.9
208.210	182.060	234.370	7197.	472.	810.	1184.	42.9
268.040	234.370	301.710	5406.	487.	734.	979.	42.9
345.050	301.710	388.400	5397.	585.	843.	1063.	42.9
444.200	388.400	500.000	4759.	662.	891.	1059.	42.9
750.000	500.000	1000.000	6258.	685.	1158.	1380.	42.9
1500.000	1000.000	2000.000	4632.	989.	1379.	1487.	42.9

Table 4. Differential number counts at 160 μm . $\sigma_{clustering}$ is uncertainty taking into account clustering (see section 4.5). $\sigma_{clus.+calib.}$ take into accounts both clustering and calibration (Stansberry et al. 2007).

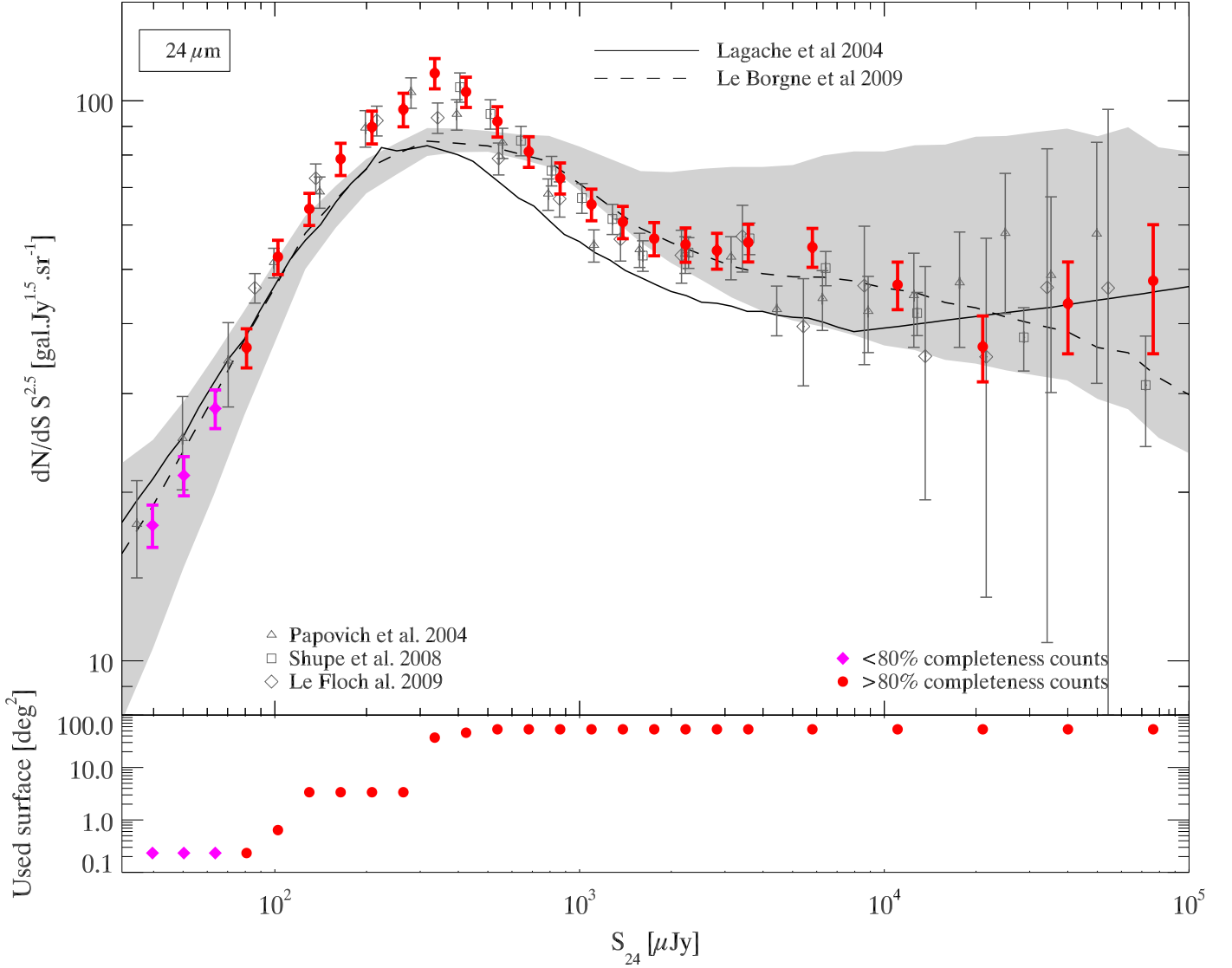


Figure 5. Differential number counts at 24 μm ; *Filled circle*: points obtained with $\geq 80\%$ completeness; *Filled diamond*: points obtained with a 50% to 80% completeness; *Open triangle*: Papovich et al. (2004) GTO number counts obtained with PSF fitting photometry; *Open square*: Shupe et al. (2008) SWIRE number counts obtained with aperture photometry; *Open diamond*: LeFloch et al. (2009) COSMOS number counts obtained with PSF fitting photometry; *Continuous line*: Lagache et al. (2004) model; *Dashed line and grey region*: Le Borgne et al. (2009) model and 90% confidence region. Error bars take into accounts clustering (see section 4.5) and calibration uncertainties (Engelbracht et al. 2007).

The uncertainties on the number counts are poissonian only if sources are distributed uniformly. But, in fact, the infrared galaxies are clustered. The uncertainties thus must be computed taking into account clustering. We firstly measure the source clustering as a function of flux density with the counts-in-cells moments (c-in-c) method (Peebles 1980; Szapudi 1998; Blake & Wall 2002). We secondly compute the uncertainties knowing these clustering properties of the sources, the source density in the flux density bins and the field shapes. The details are explained in the appendix A.

This statistical uncertainty can be combined with *Spitzer* calibration uncertainty (Engelbracht et al. 2007; Gordon et al. 2007; Stansberry et al. 2007) in order to compute total uncer-

tainty on differential number counts.

5. Deeper FIR number counts using a stacking analysis

5.1. Method

The number counts derived in section 4 show that, down to the 80% completeness limit, the source surface density is 24100, 1200, and 220 deg^{-2} at 24, 70, and 160 μm , respectively, i.e. 20 times (resp. 110 times) larger at 24 μm than at 70 μm (resp. 160 μm). These differences can be explained by the angular resolution decreasing with increasing wavelength, thus

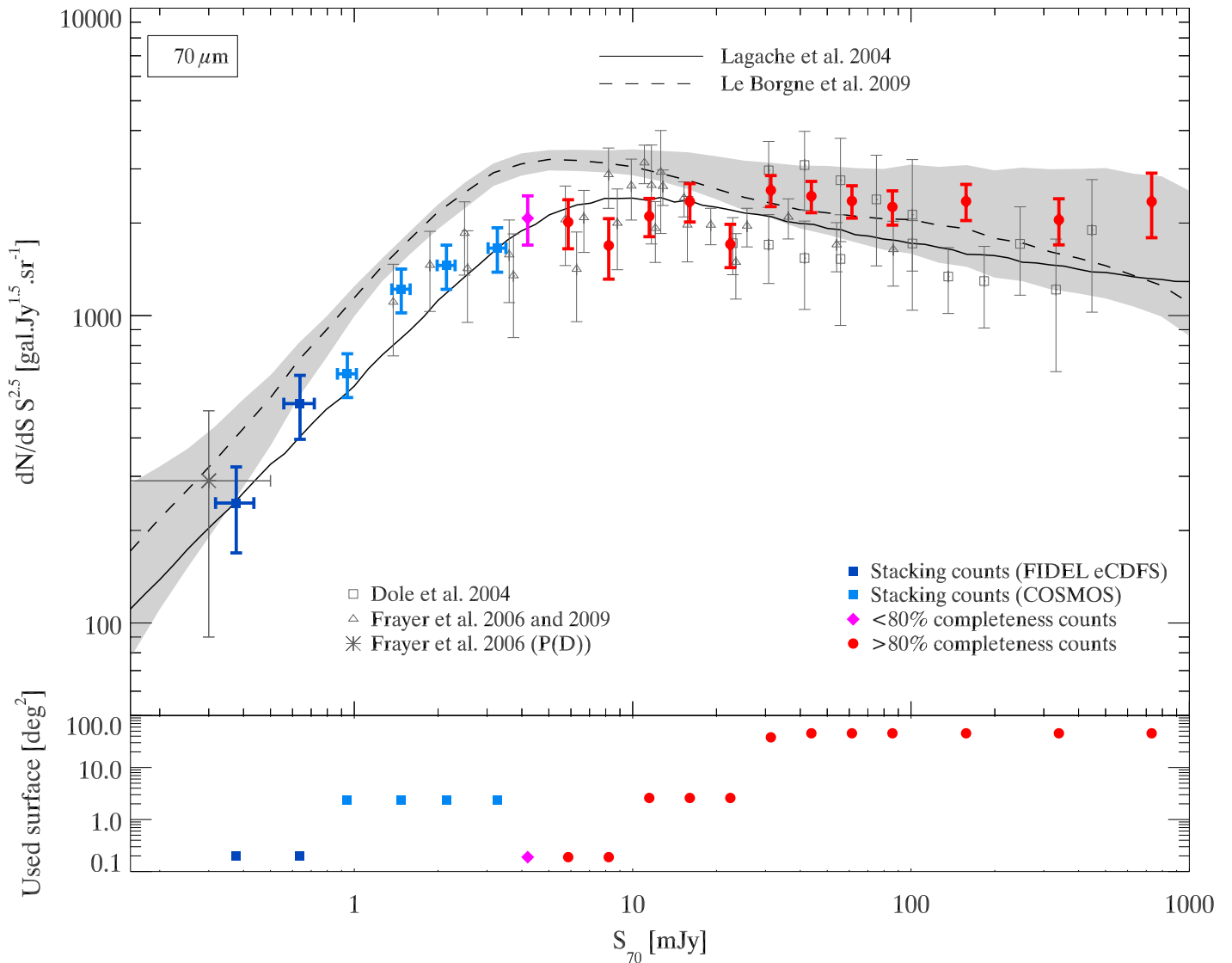


Figure 6. Differential number counts at $70\ \mu\text{m}$; *Filled circle*: points obtained with $\geq 80\%$ completeness; *Filled diamond*: points obtained with less than 50% spurious sources and less than 80% completeness; *Filled square*: Stacking number counts (clear: FIDEL eCDFS, dark: COSMOS); *Open square*: Dole et al. (2004) number counts in CDFS, Bootes and Marano; *Open triangle*: Frayer et al. (2006) in GOODS and Frayer et al. (2009) in COSMOS; *Cross*: Frayer et al. (2006) deduced from background fluctuations; *Continuous line*: Lagache et al. (2004) model; *Dashed line and grey region*: Le Borgne et al. (2009) model and 90% confidence region. Error bars take into accounts clustering (see section 4.5) and calibration uncertainties (Gordon et al. 2007).

increasing confusion, and the noise properties of the detectors. There are thus many $24\ \mu\text{m}$ sources without detected FIR counterparts. If we want to probe deeper the FIR number counts, we can take advantage of the information provided by the $24\ \mu\text{m}$ data, namely the existence of infrared galaxies not necessarily detected in the FIR, and their positions.

We use a stacking analysis (Dole et al. 2006) to determine the FIR/MIR color as a function of MIR flux. With this information, we can convert MIR counts into FIR counts. The stacking technique consists in piling up very faint far-infrared galaxies which are not detected individually, but are detected at $24\ \mu\text{m}$. For this purpose, it makes use of the $24\ \mu\text{m}$ data as a prior to track their undetected counterpart at 70 and $160\ \mu\text{m}$, where

most of the bolometric luminosity arises. This method has been used by Dole et al. (2006), who managed to resolve the FIR CIB using $24\ \mu\text{m}$ sources positions, as well as many authors (e.g Serjeant et al. (2004); Dye et al. (2006); Wang et al. (2006); Devlin et al. (2009); Dye et al. (2009); Marsden et al. (2009); Pascale et al. (2009)).

In order to derive the 70 or $160\ \mu\text{m}$ versus $24\ \mu\text{m}$ color, we stack the FIR maps (cleaned of bright sources) at the positions of $24\ \mu\text{m}$ sources sorted by flux, and perform aperture photometry (same parameters as in section 2). We thus get:

$$\overline{S_{\text{FIR}}} = f(\overline{S_{24}}) \quad (2)$$

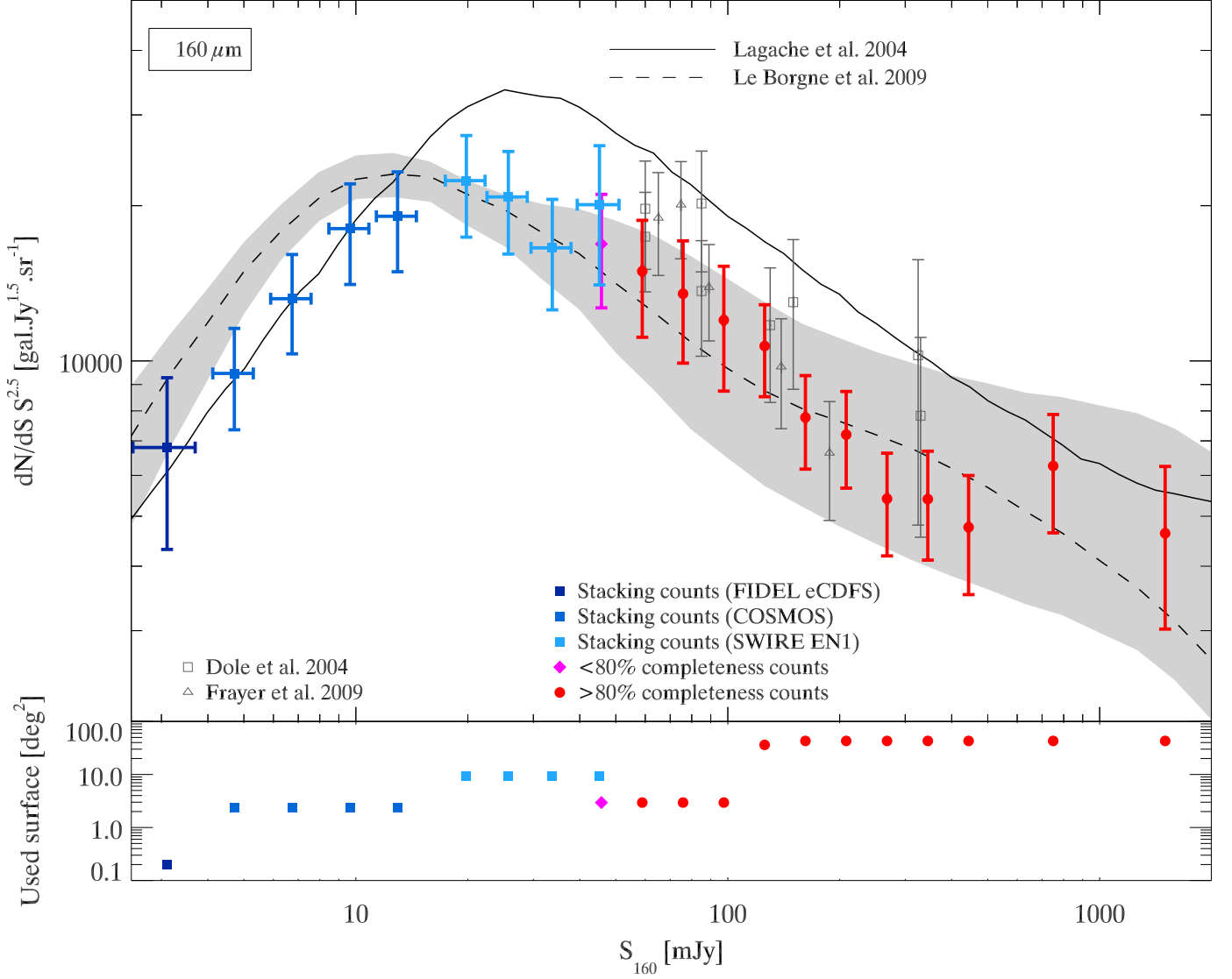


Figure 7. Differential number counts at $160\ \mu\text{m}$; *Filled circle*: points obtained with $\geq 80\%$ completeness; *Filled diamond*: points obtained with less than 50% spurious sources and less than 80% completeness; *Filled square*: Stacking number counts (clear: FIDEL/GTO CDFS, middle: COSMOS, dark: SWIRE EN1); *Open square*: Dole et al. (2004) number counts in CDFS and Marano; *Open triangle*: Frayer et al. (2009) in COSMOS; *Continuous line*: Lagache et al. (2004) model; *Dashed line and grey region*: Le Borgne et al. (2009) model and 90% confidence region. Error bars take into accounts clustering (see section 4.5) and calibration uncertainties (Stansberry et al. 2007).

where $\overline{S_{FIR}}$ is the average flux density in the FIR of the population selected at $24\ \mu\text{m}$, $\overline{S_{24}}$ the average flux density at $24\ \mu\text{m}$, and f is the function linking both quantities. We derive f empirically using S_{FIR} versus S_{24} relation obtained from stacking.

We check that f is a smooth monotonic function, in agreement with the expectation that the color varies smoothly with the redshift and the galaxy emission properties. Assuming that the individual sources follow this relation exactly, the FIR number counts could be deduced from:

$$\left. \frac{dN}{dS_{FIR}} \right|_{S_{FIR}=f(S_{24})} = \left. \frac{dN}{dS_{24}} \right|_{S_{24}} \left| \frac{dS_{FIR}}{dS_{24}} \right|_{S_{24}} \quad (3)$$

In practice, the two first terms are discrete. In addition, the last term is computed numerically in the same S_{24} bin, using the two neighboring flux density bins ($k-1$ and $k+1$). We finally get:

$$\frac{dN}{dS_{FIR}}(\overline{S_{FIRk}}) = \left(\frac{dN}{dS_{24}} \right)_k \frac{\overline{S_{FIR,k+1}} - \overline{S_{FIR,k-1}}}{\overline{S_{24,k+1}} - \overline{S_{24,k-1}}} \quad (4)$$

where $\langle S_{FIR} \rangle$ is measured by stacking. In reality, sources do not follow exactly Eq. 2, but exhibit a scatter around this mean relation:

$$S_{FIR} = f(S_{24}) + \sigma \quad (5)$$

Our method is still valid under the condition $\frac{\sigma}{f} \ll 1$, and we verify its validity using simulations (see next section).

To obtain a better signal to noise ratio, we clean the resolved bright sources from the FIR maps, prior to stack. We use $8S_{24}$ bins per decade. We stack a source only if the coverage is more than half of the median coverage of the map. Uncertainties on the FIR mean flux are estimated using a bootstrap method. Furthermore, knowing the uncertainties on the $24\ \mu\text{m}$ number counts and the mean S_{24} fluxes, we deduce the uncertainties on the FIR number counts according to Eq. 4.

At $70\ \mu\text{m}$, we use the FIDEL eCDFS (cleaned at $S_{70} > 10\ \text{mJy}$) and the COSMOS (cleaned at $S_{70} > 50\ \text{mJy}$) fields. At $160\ \mu\text{m}$, we use $160\ \mu\text{m}$ the GTO CDFS (cleaned at $S_{160} > 60\ \text{mJy}$), the COSMOS (cleaned at $S_{160} > 100\ \text{mJy}$) and the SWIRE EN1 (no clean to probe the $S_{160} > 20\ \text{mJy}$ sources) fields.

5.2. Validation on simulations

We use the Fernandez-Conde et al. (2008) simulations⁷ to validate our method. These simulations are based on the Lagache et al. (2004) model, and include galaxy clustering. We use 20 simulated mock catalogs of a $2.9\ \text{deg}^2$ field each, containing about 870 000 mock sources each. The simulated maps have the same pixel size than the actual Spitzer mosaics ($1.2''$, $4''$, and $8''$ at 24 , 70 , and $160\ \mu\text{m}$, resp.), are convolved with our empirical PSF. A constant standard deviation gaussian noise is added. We apply the same method as for real data to produce stacking number counts. At $160\ \mu\text{m}$, for bins below $15\ \text{mJy}$, we clean the sources brighter than $50\ \text{mJy}$. Figure 8 shows $160\ \mu\text{m}$ number counts from the mock catalogs down to $S_{160} = 1\ \text{mJy}$ (diamond) and the number counts deduced from the stacking analysis described in the previous section (triangle). The error bars on the figure are the standard deviations of the 20 realization. There is a good agreement between the stacking counts and the classical counts (better than 15%). Nevertheless, we observe systematic bias, intrinsic to the method, of about 10% in some flux density bins. We thus combine this 10% error with the statistical uncertainties to compute our error bars. We also validate the estimation of the statistical uncertainty in the stacking counts: we check that the dispersion of the counts obtained by stacking, coming from different realizations, is compatible with our estimation of statistical uncertainties. The results are the same at $70\ \mu\text{m}$.

5.3. Results

At $70\ \mu\text{m}$, the stacking number counts reach $0.38\ \text{mJy}$ (see figure 6 and table 5). The last stacking point is compatible with the Frayer et al. (2006) P(D) constraint. The stacking points are also in very good agreements with Lagache et al. (2004) model. The Le Borgne et al. (2009) model predicts slightly too many sources in 0.3 to $3\ \text{mJy}$ range. The turnover around $3\ \text{mJy}$ and the power law behaviour of the faint counts ($S_{70} < 2\ \text{mJy}$), observed by Frayer et al. (2006) are confirmed with a better accuracy.

At $160\ \mu\text{m}$, the stacking counts reach $3.1\ \text{mJy}$ (see figure 7 and table 6). We observe for the first time a turnover at about $20\ \text{mJy}$, and a power-law decrease at smaller flux densities. The stacking counts are lower than the Lagache et al. (2004) model

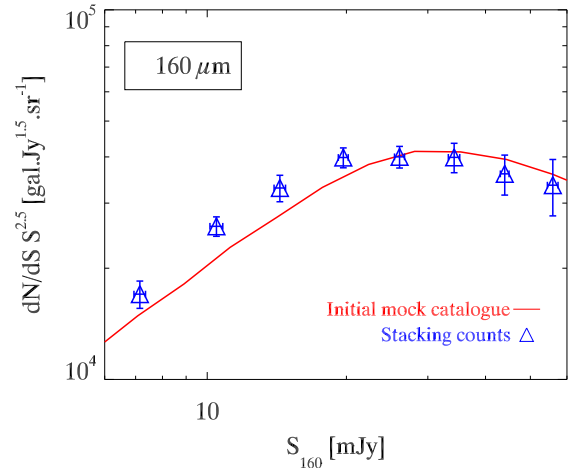


Figure 8. Simulated number counts at $160\ \mu\text{m}$, computed from stacking counts (triangle) and from the input mock catalog (solid line). The good agreement (better than 15%) validates the stacking counts method (see section 5.2). 20 realizations of $2.9\ \text{deg}^2$ field maps with about 870 000 mock sources each were used.

$\langle S \rangle$ (in mJy)	$dN/dS.S^{2.5}$ (in gal.Jy ^{1.5} .sr ⁻¹)	$\sigma_{clus.}$	$\sigma_{clus.+calib.}$	Field
0.38 ± 0.05	246.	72.	76.	FIDEL CDFS
0.64 ± 0.07	517.	109.	122.	FIDEL CDFS
0.94 ± 0.03	646.	80.	105.	COSMOS
1.48 ± 0.04	1218.	151.	198.	COSMOS
2.14 ± 0.05	1456.	183.	239.	COSMOS
3.27 ± 0.07	1657.	211.	273.	COSMOS

Table 5. Stacking extragalactic number counts et $70\ \mu\text{m}$. $\sigma_{clus.}$ is uncertainty taking into account clustering (see section 4.5). $\sigma_{clus.+calib.}$ take into accounts both clustering and calibration (Gordon et al. 2007).

$\langle S \rangle$ (in mJy)	$dN/dS.S^{2.5}$ (in gal.Jy ^{1.5} .sr ⁻¹)	$\sigma_{clus.}$	$\sigma_{clus.+calib.}$	Field
3.11 ± 0.46	6795.	2163.	2485.	GTO CDFS
4.71 ± 0.16	9458.	1236.	2104.	COSMOS
6.74 ± 0.22	13203.	1627.	2880.	COSMOS
9.65 ± 0.26	18057.	2307.	3986.	COSMOS
12.95 ± 0.37	19075.	2388.	4182.	COSMOS
19.82 ± 0.48	22366.	2944.	4987.	SWIRE EN1
25.71 ± 0.81	20798.	2811.	4682.	SWIRE EN1
33.74 ± 0.98	16567.	2671.	4004.	SWIRE EN1
45.18 ± 2.08	20089.	4849.	6049.	SWIRE EN1

Table 6. Stacking extragalactic number counts et $160\ \mu\text{m}$. $\sigma_{clus.}$ is uncertainty taking into account clustering (see section 4.5). $\sigma_{clus.+calib.}$ take into accounts both clustering and calibration (Stansberry et al. 2007).

around $20\ \text{mJy}$ (about 30%). Below $15\ \text{mJy}$, the stacking counts are in agreement with this model. The Le Borgne et al. (2009) model is in quite good agreement with our points below $20\ \text{mJy}$. The results at $160\ \mu\text{m}$ will be discussed in section 7.2.

⁷ Publicly available at <http://www.ias.u-psud.fr/irgalaxies/>

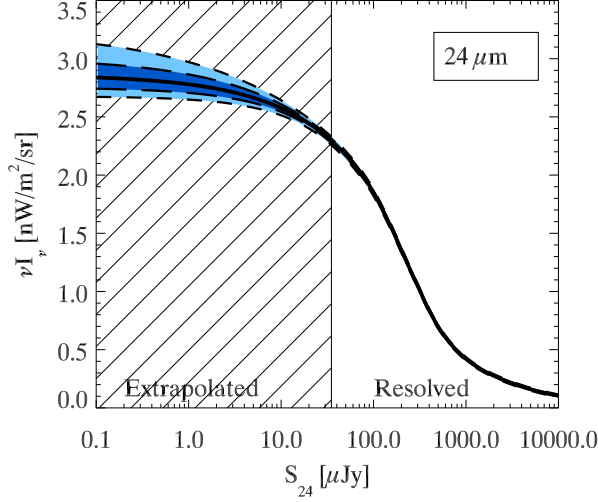


Figure 9. Cumulative contribution to the surface brightness of the 24 μm CIB as a function of $S_{24\mu\text{m}}$. colored area represent 68% and 95% confidence level. Shaded area represents the $S_{24} < 35\mu\text{Jy}$ power-law extrapolation zone (see section 6.1). The 4% calibration uncertainty is not represented. The table corresponding to this figure is available online at <http://www.ias.u-psud.fr/irgalaxies/>.

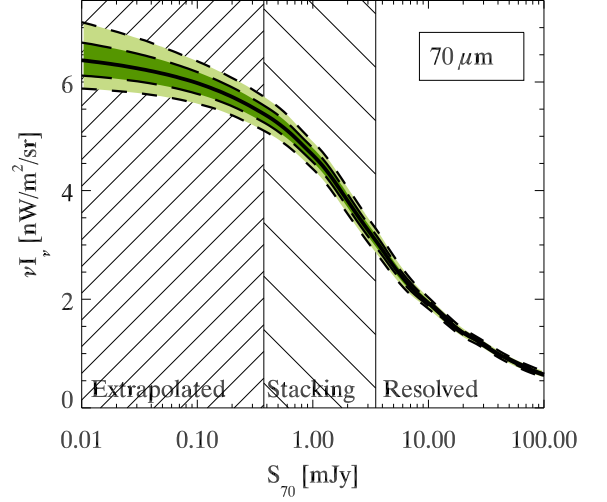


Figure 10. Cumulative contribution to the surface brightness of the 70 μm CIB as a function of $S_{70\mu\text{m}}$. colored area represent 68% and 95% confidence level. Shaded areas represent the $0.38 < S_{70} < 3.3$ mJy stacking counts zone, and the $S_{70} < 0.38$ mJy power-law extrapolation zone (see section 6.2). The 7% calibration uncertainty is not represented. The table corresponding to this figure is available online at <http://www.ias.u-psud.fr/irgalaxies/>.

6. New lower limits and estimates of the CIB at 24, 70 and 160 μm

6.1. 24 μm CIB: lower limit and estimate

By integrating the measured 24 μm number counts between 35 μJy and 0.1 Jy, we can estimate a lower value of the CIB at this wavelength. The counts are integrated using a trapeze method. We estimate the uncertainty on the integral by adding (on 10000 realisations) to each data point a random gaussian error with the σ given by the counts uncertainties taking into account clustering. We then add the 4% calibration error of instrument (Engelbracht et al. 2007). We find $2.26^{+0.09}_{-0.09}$ $\text{nW.m}^{-2}.\text{sr}^{-1}$. The very bright source counts ($S_{24} > 0.1$ Jy) are supposed to be euclidian ($dN/dS = C_{\text{eucl}}S^{2.5}$). We use the three brightest points to estimate C_{eucl} . We find a contribution to the CIB of $0.032^{+0.003}_{-0.003}$ $\text{nW.m}^{-2}.\text{sr}^{-1}$. Consequently, very bright sources extrapolation is not critical for the CIB estimation (1% of CIB). The contribution of $S_{24} > 35 \mu\text{Jy}$ is thus $2.29^{+0.09}_{-0.09}$ $\text{nW.m}^{-2}.\text{sr}^{-1}$ (c.f. table 7).

We might want to estimate the CIB value at 24 μm ; To do so, we need to extrapolate the number counts on the faint end. Below 100 μJy , the number counts exhibit a power-law behaviour (fig. 5). We assume that this behaviour (of the form $dN/dS = C_{\text{faint}}S^r$) still holds below 35 μJy . r and C_{faint} are determined using the four faintest bins. We find $r = 1.45 \pm 0.10$ (compatible with 1.5 ± 0.1 of Papovich et al. (2004)). Our new estimate of the CIB at 24 μm due to infrared galaxies is thus $2.86^{+0.19}_{-0.16}$ $\text{nW.m}^{-2}.\text{sr}^{-1}$. The results are plotted in figure 9. We conclude that resolved sources down to $S_{24} = 35\mu\text{Jy}$ account for 80% of the CIB at this wavelength.

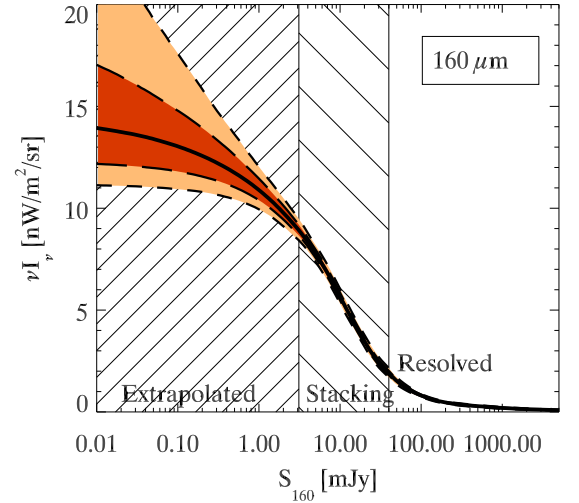


Figure 11. Cumulative contribution to the surface brightness of the 160 μm CIB as a function of $S_{160\mu\text{m}}$. colored area represent 68% and 95% confidence level. Shaded areas represent the $3.1 < S_{160} < 45$ mJy stacking counts zone, and the $S_{160} < 3.1$ mJy power-law extrapolation zone (see section 6.2). The 12% calibration uncertainty is not represented. The table corresponding to this figure is available online at <http://www.ias.u-psud.fr/irgalaxies/>.

6.2. 70 and 160 μm CIB: lower limit and estimate

At 70 and 160 μm , the integration of the number counts is done in the same way as at 24 μm , except for the stacking counts, which are correlated. To compute the uncertainties on the integral, we add (on 10000 realisations) a gaussian error simul-

		24 μm	70 μm	160 μm
$S_{\text{cut,resolved}}$	mJy	0.035	3.50	40.0
$S_{\text{cut,stacking}}$		-	0.38	3.1
$\nu B_{\nu,\text{resolved}}$	$\text{nW.m}^{-2}.\text{sr}^{-1}$	$2.29^{+0.09}_{-0.09}$	$3.1^{+0.2}_{-0.2}$	$1.0^{+0.1}_{-0.1}$
$\nu B_{\nu,\text{resolved+stacking}}$		-	$5.4^{+0.4}_{-0.4}$	$8.9^{+1.1}_{-1.1}$
$\nu B_{\nu,\text{tot}}$		$2.86^{+0.19}_{-0.16}$	$6.6^{+0.7}_{-0.6}$	$14.6^{+7.1}_{-2.9}$

Table 7. Summary of CIB results found in this article.

taneously to the three quantities and completely recompute the associated stacking counts: 1- the mean density flux given by the stacking; 2- the 24 μm number counts; 3- the mean 24 μm flux density. At 70, and 160 μm , the calibration uncertainty is 7 % (Gordon et al. 2007), and 12% (Stansberry et al. 2007), respectively. We estimate the CIB surface brightness contribution of resolved sources ($S_{70} > 3.5$ mJy and $S_{160} > 40$ mJy) of $3.1^{+0.2}_{-0.2}$, and $1.0^{+0.1}_{-0.1}$ $\text{nW.m}^{-2}.\text{sr}^{-1}$. The contribution of $S_{70} > 0.38$ mJy, and $S_{160} > 3.1$ mJy) is $5.4^{+0.4}_{-0.4}$, and $8.9^{+1.1}_{-1.1}$ $\text{nW.m}^{-2}.\text{sr}^{-1}$, respectively.

Below 2 mJy at 70 μm , and 10 mJy at 160 μm , the stacking counts are compatible with a power-law. Like at 24 μm , we assume that this behaviour can be extrapolated and determine the law with the five faintest bins at 70 μm , and the four faintest at 160 μm . We find a slope $r = 1.50 \pm 0.14$ at 70 μm , and 1.61 ± 0.21 at 160 μm . The slope of the number counts at 70 μm is compatible with Frayer et al. (2006) value (1.63 ± 0.34). The slope at 160 μm is measured for the first time. Our new estimate of the CIB at 70, and 160 μm due to infrared galaxies is thus $6.6^{+0.7}_{-0.6}$, and $14.6^{+7.1}_{-2.9}$ $\text{nW.m}^{-2}.\text{sr}^{-1}$, respectively. We conclude that resolved and stacking-studied populations account for 82%, and 62% of the CIB at 70, and 160 μm , respectively. These results are summarised in table 7, and figures 10 and 11.

7. Discussion

7.1. New lower limits of the CIB

The estimations of CIB based on number counts ignore a potential diffuse infrared emission, like dust in galaxy clusters (Montier & Giard 2005). The extrapolation of the faint source counts suppose no low luminosity population, like population III stars or faint unseen galaxies. So, this type of measurement can provide only a lower limit in principle.

At 24 μm , Papovich et al. (2004) found $2.7^{+0.7}_{-1.1}$ $\text{nW.m}^{-2}.\text{sr}^{-1}$ using the counts and the extrapolation of the faint source counts. We are in agreement with this work and we significantly reduce the uncertainties on this estimation. Dole et al. (2006) found a contribution of 1.93 ± 0.23 $\text{nW.m}^{-2}.\text{sr}^{-1}$ for $S_{24} > 60 \mu\text{Jy}$ sources (after dividing their results by 1.12 to correct an aperture error in their photometry at 24 μm). Our analysis gives 2.10 ± 0.08 $\text{nW.m}^{-2}.\text{sr}^{-1}$ for a cut at 60 μJy , in excellent agreement. Rodighiero et al. (2006) gave a total value of 2.6 $\text{nW.m}^{-2}.\text{sr}^{-1}$, without any error bar. Chary et al. (2004) found 2.0 ± 0.2 $\text{nW.m}^{-2}.\text{sr}^{-1}$, by integrating sources between 20 and 1000 μJy (we find 2.02 ± 0.10 for the same interval).

At 70 μm , using the number counts in the ultra deep GOODS-N and a P(D) analysis, Frayer et al. (2006) found a $S_{70} > 0.3$ mJy source contribution to the 70 μm CIB of 5.5 ± 1.1 $\text{nW.m}^{-2}.\text{sr}^{-1}$. Using the stacking counts, we find

5.5 ± 0.4 $\text{nW.m}^{-2}.\text{sr}^{-1}$ for the same cut, in excellent agreement and with improved uncertainties. In Dole et al. (2006), the contribution at 70 μm of the $S_{24} < 60 \mu\text{Jy}$ sources was computed using an extrapolation of the 24 μm number counts and the 70/24 color. They found 7.1 ± 1.0 $\text{nW.m}^{-2}.\text{sr}^{-1}$, but the uncertainty on the extrapolation took only into account the uncertainty on the 70/24 color and not the uncertainty on the extrapolated 24 μm contribution, and was thus slightly underestimated. This is in agreement with our estimation.

At 160 μm , they found, with the same method, 17.4 ± 2.1 $\text{nW.m}^{-2}.\text{sr}^{-1}$ (a corrective factor of 1.3 is applied due to an error on the map pixel size). This estimation is a little bit higher than our estimation, and can be explained by a small contribution (at the order of 15%) of the source clustering (Bavouzet 2008).

Our results can also be compared with direct measurements made by absolute photometers. These methods are biased by the foreground modeling, but do not ignore the extended emission. Fixsen et al. (1998) have found a CIB brightness of 13.7 ± 3.0 at 160 μm , in excellent agreement with our estimation ($14.6^{+7.1}_{-2.9}$ nW.m^{-2}). From the discussion in Dole et al. (2006) (section 4.1), the Lagache et al. (2000) DIRBE WHAM (FIRAS calibration) estimation at 140 and 240 μm of 12 and 12.2 $\text{nW.m}^{-2}.\text{sr}^{-1}$ can be also compared with our value at 160 μm . A more recent work of Odegard et al. (2007) has found 25.0 ± 6.9 and 13.6 ± 2.5 $\text{nW.m}^{-2}.\text{sr}^{-1}$ at 140 and 240 μm respectively (resp. 15 ± 5.9 and 12.7 ± 1.6 $\text{nW.m}^{-2}.\text{sr}^{-1}$ with FIRAS scale). Using ISOPHOT data, Juvela et al. (2009) give an estimation of the CIB surface brightness between 150 and 180 μm of $20.25 \pm 6.0 \pm 5.6$ $\text{nW.m}^{-2}.\text{sr}^{-1}$.

The total brightness due to infrared galaxies at 160 μm correspond to the total CIB level at this wavelength. We thus have probably resolved the CIB at this wavelength. Nevertheless, the uncertainties are relatively large, and other minor CIB contributors cannot be excluded.

In addition, upper limits can be deduced indirectly from blazar high energy spectrum. Stecker & de Jager (1997) give an upper limit of 4 $\text{nW.m}^{-2}.\text{sr}^{-1}$ at 20 μm using Mkn 421. Renault et al. (2001) find an upper limit of 4.7 $\text{nW.m}^{-2}.\text{sr}^{-1}$ between 5 and 15 μm with Mkn 501. This is consistent with our lower limit at 24 μm .

An update of the synthetic EBL SED of Dole et al. (2006) with the new BLAST (Balloon-borne Large-Aperture Submillimeter Telescope) lower limits from Devlin et al. (2009) and our values is plotted in figure 12. The BLAST lower limits are obtained by stacking of the *Spitzer* 24 μm sources at 250, 350 and 500 μm (Devlin et al. 2009; Marsden et al. 2009).

7.2. 160 μm number counts

At most, we observe a 30% overestimation of the Lagache et al. (2004) model compared to the 160 μm number counts (sections 4.4 and 5.3 and figure 7), despite good fits at other wavelengths. This model uses mean SEDs of galaxies sorted in two populations (starburst and cold), whose luminosity functions evolve separately with the redshift. A possible explanation of the model excess is a slightly too high density of local cold galaxies. By decreasing a bit the density of this local population, the model

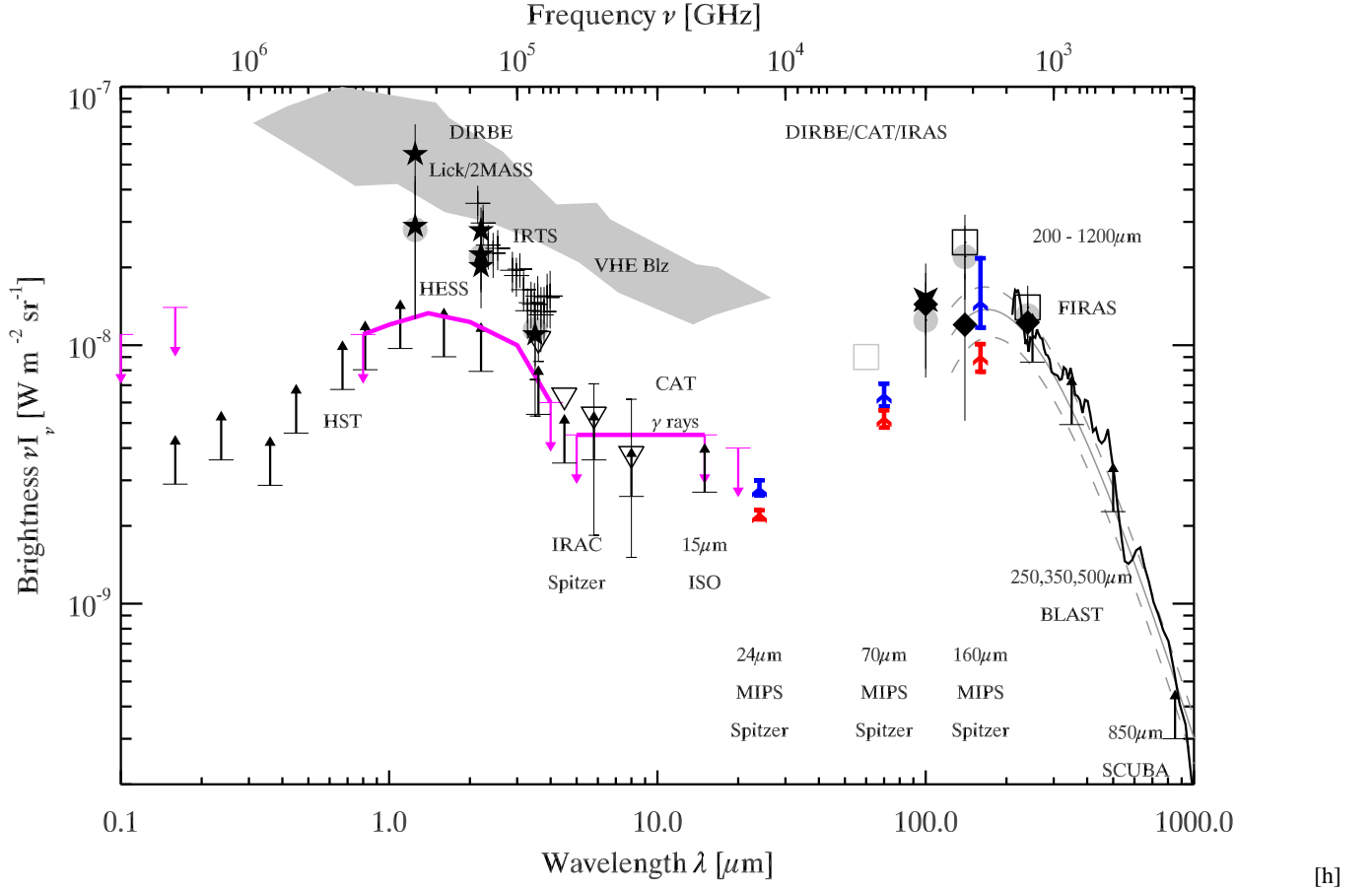


Figure 12. Current measurement of extragalactic background light spectral energy distribution from 100 nm to 1mm, with the Cosmic Optical Background (COB, $\lambda < 8 \mu\text{m}$) and Cosmic Infrared Background (CIB, $\lambda > 8 \mu\text{m}$). Our new points at 24, 70 and 160 μm are plotted (*triangle*). Lower (red) triangles correspond to the CIB resolved with the number counts and stacking counts. Upper (blue) triangles correspond to the total extrapolated CIB due to infrared galaxies. BLAST lower limits at 250, 350 and 500 μm (Devlin et al. 2009; Marsden et al. 2009) are represented in *black arrows*. The FIRAS measurements of Fixsen et al. (1998) between 125 and 2000 μm are plotted with a *grey solid line*, and the 1- σ confidence region with a *grey dashed line*. Other points come from different authors (see Dole et al. (2006) for complete details). Old MIPS points are not plotted in order to have a clearer plot.

might be able to better fit the 160 μm number counts without affecting significantly other wavelengths, especially at 70 μm (more sensitive to warm dust rather than cold dust), and in the submillimetre range (more sensitive to redshifted cold dust at faint flux densities for wavelength larger than 500 μm).

The Le Borgne et al. (2009) model slightly overpredicts faint 160 μm sources, probably because of the presence of too many galaxies at high redshift; this trend is also seen at 70 μm . With our number counts as new constraints, their inversion should give more accurate parameters.

Herschel was successfully launched on May 14th, 2009 (together with *Planck*). It will observe infrared galaxies between 70 and 500 μm with an improved sensitivity. It will be possible to observe directly cold dust spectrum of high- z ULIRG and medium- z LIRG. PACS (Photodetectors Array Camera and Spectrometer) will make photometric surveys in 3 bands centred on 70, 100 and 160 μm . *Herschel* will allow to resolve a significant fraction of the background at these wavelengths (Lagache et al. 2003; Le Borgne et al. 2009). SPIRE (Spectral and Photometric Imaging Receiver) will observe around 250, 350 and 500 μm , and will be quickly confusion limited. In

both case, the stacking analysis will allow to probe fainter flux density levels, being complementary to *Spitzer* and BLAST.

8. Conclusion

Using a large sample of public *Spitzer* extragalactic maps, we have build new deep, homogeneous, high-statistics number counts in 3 MIPS bands at 24, 70 and 160 μm .

At 24 μm , the results are in agreement with previous works. These counts are derived from the widest surface ever used at this wavelength (53.6 deg²). Using these counts, we give an accurate estimation of the galaxy contribution to the CIB at this wavelength ($2.86^{+0.19}_{-0.16} \text{ nW.m}^{-2}.\text{sr}^{-1}$).

At 70 μm , we use the stacking method to determine the counts below the detection limit of individual sources, by reaching 0.38 mJy, allowing to probe the faint flux density slope of differential number counts. Using this information, we deduce the total contribution of galaxies to the CIB at this wavelength ($6.6^{+0.7}_{-0.6} \text{ nW.m}^{-2}.\text{sr}^{-1}$).

At 160 μm , our counts reach 3 mJy using a stacking analysis. We exhibit for the first time the maximum in differential number counts around 20 mJy and the power-law behaviour below 10 mJy. We deduce the total contribution of galaxies to the CIB at this wavelength ($14.6^{+7.1}_{-2.9} nW.m^{-2}.sr^{-1}$). *Herschel* will likely probe flux densities down to about 10 mJy at this wavelength (confusion limit, Le Borgne et al. (2009)).

The uncertainties on the number counts used in this work take carefully into account the galaxy clustering, which is measured with the "counts-in-cells" method.

We have presented a method to build very deep number counts using the information provided by shorter wavelength data (MIPS 24 μm) and a stacking analysis. This tool might be used on *Herschel* SPIRE data with a PACS prior, in order to probe fainter flux densities in the submillimetre range.

We publicly release on the website <http://www.ias.u-psud.fr/irgal/>, the following products: PSF, number counts and CIB contributions. We also release a stacking library software written in IDL.

Acknowledgements. We want to acknowledge G. Lagache, who has generated simulations used in this work. We acknowledge J.L. Puget, G. Lagache, D. Marcillac, B. Bertin, A. Penin and all members of cosmology group of IAS for their comments and suggestions. We want to thank the members of ANR D-SIGALE for their precious comments, in particular D. Le Borgne for providing us an electronic version of his model. We also thank E. Le Floch for quickly providing us the table of his counts. This work is based in part on archival data obtained with the Spitzer Space Telescope, which is operated by the Jet Propulsion Laboratory, California Institute of Technology under a contract with NASA. Support for this work was provided by an award issued by JPL/Caltech. This publication makes use of data products from the Two Micron All Sky Survey, which is a joint project of the University of Massachusetts and the Infrared Processing and Analysis Center/California Institute of Technology, funded by the National Aeronautics and Space Administration and the National Science Foundation.

References

- Arendt, R. G., Odegard, N., Weiland, J. L., et al. 1998, *ApJ*, 508, 74
 Bavouzet, N. 2008, PhD thesis, Universit   Paris-Sud 11 <http://tel.archives-ouvertes.fr/tel-00363975/>
 Bertin, E. & Arnouts, S. 1996, *A&AS*, 117, 393
 Blake, C. & Wall, J. 2002, *MNRAS*, 337, 993
 Chary, R., Casertano, S., Dickinson, M. E., et al. 2004, *ApJS*, 154, 80
 Devlin, M. J., Ade, P. A. R., Aretxaga, I., et al. 2009, *Nature*, 458, 737
 Diolaiti, E., Bendinelli, O., Bonaccini, D., et al. 2000, *A&AS*, 147, 335
 Dole, H., Gispert, R., Lagache, G., et al. 2001, *A&A*, 372, 364
 Dole, H., Lagache, G., & Puget, J.-L. 2003, *ApJ*, 585, 617
 Dole, H., Lagache, G., Puget, J.-L., et al. 2006, *A&A*, 451, 417
 Dole, H., Le Floch, E., P  rez-Gonz  lez, P. G., et al. 2004, *ApJS*, 154, 87
 Dye, S., Ade, P. A. R., Bock, J. J., et al. 2009, *ApJ*, 703, 285
 Dye, S., Eales, S. A., Ashby, M. L. N., et al. 2006, *ApJ*, 644, 769
 Eddington, A. S. 1913, *MNRAS*, 73, 359
 Eddington, Sir, A. S. 1940, *MNRAS*, 100, 354
 Elbaz, D., Cesarsky, C. J., Chailal, P., et al. 2002, *A&A*, 384, 848
 Engelbracht, C. W., Blaylock, M., Su, K. Y. L., et al. 2007, *PASP*, 119, 994
 Fernandez-Conde, N., Lagache, G., Puget, J.-L., & Dole, H. 2008, *A&A*, 481, 885
 Fixsen, D. J., Dwek, E., Mather, J. C., Bennett, C. L., & Shafer, R. A. 1998, *ApJ*, 508, 123
 Franceschini, A., Rodighiero, G., Vaccari, M., Marchetti, L., & Mainetti, G. 2009, *ArXiv e-prints*
 Frayer, D. T., Huynh, M. T., Chary, R., et al. 2006, *ApJ*, 647, L9
 Frayer, D. T., Sanders, D. B., Surace, J. A., et al. 2009, *AJ*, 138, 1261
 Gispert, R., Lagache, G., & Puget, J. L. 2000, *A&A*, 360, 1
 Gordon, K. D., Engelbracht, C. W., Fadda, D., et al. 2007, *PASP*, 119, 1019
 Hauser, M. G., Arendt, R. G., Kelsall, T., et al. 1998, *ApJ*, 508, 25
 Hauser, M. G. & Dwek, E. 2001, *ARA&A*, 39, 249

- Juvela, M., Mattila, K., Lemke, D., et al. 2009, *A&A*, 500, 763
 Kashlinsky, A. 2005, *Phys. Rep.*, 409, 361
 Krist, J. 2006, *Tiny Tim/Spitzer User's Guide*
 Lagache, G., Abergel, A., Boulanger, F., D  sert, F. X., & Puget, J.-L. 1999, *A&A*, 344, 322
 Lagache, G., Dole, H., & Puget, J.-L. 2003, *MNRAS*, 338, 555
 Lagache, G., Dole, H., Puget, J.-L., et al. 2004, *ApJS*, 154, 112
 Lagache, G., Haffner, L. M., Reynolds, R. J., & Tufte, S. L. 2000, *A&A*, 354, 247
 Lagache, G., Puget, J.-L., & Dole, H. 2005, *ARA&A*, 43, 727
 Le Borgne, D., Elbaz, D., Ocvirk, P., & Pichon, C. 2009, *A&A*, 504, 727
 LeFloch, E., Aussel, H., Ilbert, O., et al. 2009, *ApJ*, 703, 222
 Marsden, G., Ade, P. A. R., Bock, J. J., et al. 2009, *ArXiv e-prints*
 Montier, L. A. & Giard, M. 2005, *A&A*, 439, 35
 Odegard, N., Arendt, R. G., Dwek, E., et al. 2007, *ApJ*, 667, 11
 Papovich, C., Dole, H., Egami, E., et al. 2004, *ApJS*, 154, 70
 Pascale, E., Ade, P. A. R., Bock, J. J., et al. 2009, *ArXiv e-prints*
 Pearson, C. & Khan, S. A. 2009, *MNRAS*, 399, L11
 Peebles, P. J. E. 1980, *The large-scale structure of the universe*
 Puget, J.-L., Abergel, A., Bernard, J.-P., et al. 1996, *A&A*, 308, L5+
 Renault, C., Barrau, A., Lagache, G., & Puget, J.-L. 2001, *A&A*, 371, 771
 Rieke, G. H., Young, E. T., Engelbracht, C. W., et al. 2004, *ApJS*, 154, 25
 Rodighiero, G., Lari, C., Pozzi, F., et al. 2006, *MNRAS*, 371, 1891
 Rowan-Robinson, M. 2009, *MNRAS*, 394, 117
 Serjeant, S., Mortier, A. M. J., Ivison, R. J., et al. 2004, *ApJS*, 154, 118
 Shupe, D. L., Rowan-Robinson, M., Lonsdale, C. J., et al. 2008, *AJ*, 135, 1050
 Skrutskie, M. F., Cutri, R. M., Stiening, R., et al. 2006, *AJ*, 131, 1163
 Stansberry, J. A., Gordon, K. D., Bhattacharya, B., et al. 2007, *PASP*, 119, 1038
 Starck, J. L., Aussel, H., Elbaz, D., Fadda, D., & Cesarsky, C. 1999, *A&AS*, 138, 365
 Stecker, F. W. & de Jager, O. C. 1997, *ApJ*, 476, 712
 Stetson, P. B. 1987, *PASP*, 99, 191
 Szapudi, I. 1998, *ApJ*, 497, 16
 Valiante, E., Lutz, D., Sturm, E., Genzel, R., & Chapin, E. 2009, *ArXiv e-prints*
 Wall, J. V. & Jenkins, C. R. 2003, *Practical Statistics for Astronomers*
 Wang, W.-H., Cowie, L. L., & Barger, A. J. 2006, *ApJ*, 647, 74
 Werner, M. W., Gallagher, D. B., & Irace, W. R. 2004, *Advances in Space Research*, 34, 600

Appendix A: Uncertainties on number counts including clustering

A.1. Counts-in-cells moments

We consider a clustered population with a surface density ρ . The expected number of object in a field of size Ω is $\bar{N} = \rho\Omega$. In the poissonian case, the standard deviation around this value is $\sqrt{\bar{N}}$. For a clustered distribution, the standard deviation σ_N is given by (Wall & Jenkins 2003):

$$\sigma_N = \sqrt{y \cdot \bar{N}^2 + \bar{N}} \quad (\text{A.1})$$

The expected value of y is given by (Peebles 1980):

$$y = \frac{\int_{\text{field}} \int_{\text{field}} w(\theta) d\Omega_1 d\Omega_2}{\Omega^2} \quad (\text{A.2})$$

where $w(\theta)$ is the angular 2 points auto correlation function of the sources.

A.2. Measuring source clustering as a function of flux density

We suppose the classical power-law description: $w(\theta) = A(S, \lambda)\theta^{1-\gamma}$ with an index $\gamma = 1.8$. So, y depends only of A and of the shape of the field:

$$y = A(S, \lambda) \frac{\int_{\text{field}} \int_{\text{field}} \theta^{1-\gamma} d\Omega_1 d\Omega_2}{\Omega^2} \quad (\text{A.3})$$

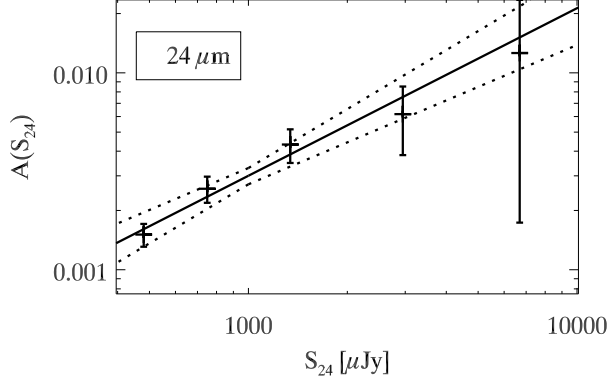


Figure A.1. Amplitude of auto correlation as a function of flux density of sources at 24 μm , and best power-law fit.

The uncertainty on y is given by (Szapudi 1998):

$$\sigma_y = \sqrt{\frac{2}{N_{\text{cell}} \bar{N}^2}} \quad (\text{A.4})$$

To measure $A(S, \lambda)$, we cut our fields in $30' \times 30'$ square boxes, in which we count the number of sources and compute the variance, in 5 (respectively 3 and 3) flux density bins at 24 μm (resp. at 70 and 60 μm). We calculate the associate $A(S, \lambda)$ combining equation A.1 and A.3:

$$A(S, \lambda) = \frac{\sigma_N^2 - \bar{N}}{\bar{N}^2} \times \frac{\Omega^2}{\int_{\text{field}} \int_{\text{field}} \theta^{1-\gamma} d\Omega_1 d\Omega_2} \quad (\text{A.5})$$

The fit of $A(S_{24}, 24\mu\text{m})$ versus S_{24} (see figure A.1) gives ($\chi^2 = 2.67$ for 5 points and 2 fitted parameters):

$$A(S, 24\mu\text{m}) = (2.86 \pm 0.29) \cdot 10^{-3} \left(\frac{S}{1\text{mJy}} \right)^{0.90 \pm 0.15} \quad (\text{A.6})$$

The measured exponent in A.6 of 0.90 ± 0.15 corresponds to $\gamma/2$, which is the expected value in the case of a flux-limited survey in an euclidean universe filled with single luminosity sources. We fix this exponent to fit $A(S_{70}, 70\mu\text{m})$ and $A(S_{160}, 160\mu\text{m})$. We find $A(1\text{mJy}, 70\mu\text{m}) = (0.25 \pm 0.08) \cdot 10^{-3}$ and $A(1\text{mJy}, 160\mu\text{m}) = (0.3 \pm 0.03) \cdot 10^{-3}$.

A.3. Compute uncertainties due to clustering

Using this model of $A(S, \lambda)$ and the field shape, we compute y (Eq. A.3). Assuming $\bar{N} = N$ (N being the number of detected sources in a given field and flux density bin), we deduce $\sigma(N)$ from Eq. A.1, and consequently the error bar on the number counts for a single field.

To compute the final uncertainty on the combined counts, we use the following relation:

$$\sigma_{\text{comb}, \frac{dN}{dS}} = \frac{\sqrt{\sum_i \Omega_i^2 \sigma_{i, \frac{dN}{dS}}^2}}{\sum_i \Omega_i} \quad (\text{A.7})$$

where $\sigma_{\text{comb}, \frac{dN}{dS}}$ is the uncertainty on the combined number counts, Ω_i the solid angle of the i -th field, and $\sigma_{i, \frac{dN}{dS}}$ the uncertainty on the number counts in the i -th field (given by $\text{Var}(N)$,

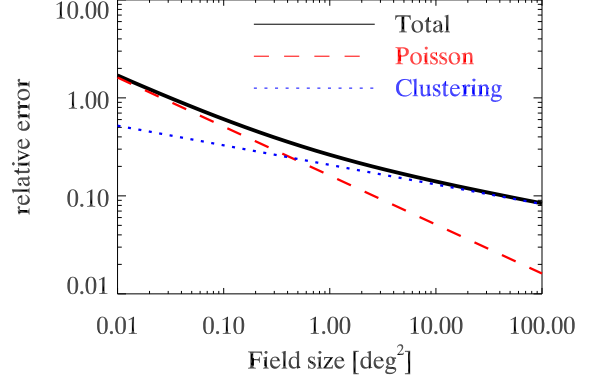


Figure A.2. Relative error on number count as a function of field size. We have chosen $A = 0.019$ and $\rho = 38.5 \text{ deg}^{-2}$ (values for a 80-120 mJy flux density bin at 160 μm). Field is a square.

Eq. A.1).

A.4. Discussion about clustering and number counts uncertainties

For clustered distribution of sources, the uncertainties on the number counts are driven by two terms combined quadratically (Eq. A.1): a poissonian term \sqrt{N} and a clustering term $\sqrt{y} \cdot N$ (see figure A.2). We have $N \propto \Omega$ and $y \propto \Omega^{(\gamma-1)/2}$ (Blake & Wall 2002). When the uncertainty is dominated by the poissonian term (small field), the relative uncertainty is thus proportional to $\sqrt{\Omega}^{-1/2}$. When the uncertainty is dominated by the clustering term (large field), the relative error is proportional to $\Omega^{(1-\gamma)/4}$ ($\Omega^{-0.2}$ for $\gamma = 1.8$).

Consequently uncertainties decrease very slowly in the the clustering regime. Averaging many small independent fields gives more accurate counts than a big field covering the same surface. For example, in the clustering regime, if a field of 10 deg^2 has a relative uncertainty of 0.2, the relative uncertainty is $0.2/\sqrt{10} = 0.063$ for the mean of 10 fields of this size, and $0.2 \times 10^{-0.2} = 0.126$ for a single field of 100 deg^2 . Consequently, if you study the counts only, lot of small fields give better results than a very large field. But, it is not optimal if you study the spatial properties of the galaxies, which requires large fields.